ChemComm

Check for updates

Atomic-scale insights into the Cu ion distribution in zeolites used for ammonia selective catalytic reduction during early hydrothermal degradation

Masahiko Shimizu, [ID] *[abc] Katsuaki Nakazawa, [ID] [d] Hisashi Shima,[a]
Hajime Matsumoto,[ab] Takahiko Takewaki,[a] Kazutaka Mitsuishi [ID] *[d] and
Ayako Hashimoto [ID] *[bc]

Early hydrothermal degradation of Cu-SSZ-13 and Cu-SSZ-39 zeolites with similar Cu content was investigated. Electron ptychography revealed the Cu occupancy at the eight-membered ring sites of Cu-SSZ-39 is lower than that of Cu-SSZ-13, clearly demonstrating that the former is more stable than the latter under hydrothermal aging conditions.

Ammonia selective catalytic reduction (NH_3-SCR) is a key exhaust purification technology for diesel vehicles that uses a commercial catalyst, Cu-SSZ-13 zeolite with the CHA topology.[1–3] The catalyst performance declines considerably after hydrothermal aging (HTA) above 800 °C. This problem remains unresolved despite extensive research.[4–10] However, Cu-SSZ-39 with the AEI topology has high hydrothermal stability and is regarded as a promising alternative.[11,12] Generally, the stability of Cu-exchange zeolites is influenced by several factors, such as the zeolite framework, Si/Al ratio, and Cu loading.[5,7,9,13] The hydrothermal stability of Cu-exchange zeolites is greater for the AEI topology than the CHA topology and increases as the Si/Al ratio and Cu loading decrease.[5,7,11] Mechanistically, degradation is thought to involve dealumination and the redistribution of Cu ions, leading to the formation of CuO_x clusters and collapse of the zeolite framework.[6–9] Although these processes originate at the atomic scale, previous analyses have relied on spatially averaged data obtained using techniques such as X-ray diffraction (XRD) and spectroscopy.[14,15] Thus, the atomic-level mechanisms remain poorly understood.

Transmission electron microscopy (TEM) enables direct observation at the atomic scale.[16,17] However, zeolites are very easily damaged by an electron beam.[18,19] This sensitivity is particularly pronounced in Al-rich catalytic zeolites, necessitating a drastic reduction in the electron dose applied.[20] Consequently, it remains difficult to observe the degraded structure of NH_3-SCR catalysts at the atomic level, often limiting observation to nanometer-scale Cu aggregates.[5] Electron ptychography[21–23] has emerged as a promising low-dose technique to overcome this limitation. This technique has been applied to various beam-sensitive materials, including zeolite.[24–32] We previously used this technique to visualize Cu ions in Cu-SSZ-13.[33,34] Building on this foundation, our primary goal in this study was to uncover the atomic-scale origins of hydrothermal stability in Cu-exchanged zeolites.

To achieve this goal, we investigated two strategically chosen zeolites with comparable Cu loadings (4.2–4.7 wt%): Cu-SSZ-39 (AEI; Si/Al = 5.2, Cu/Al = 0.29) and Cu-SSZ-13 (CHA; Si/Al = 12.6, Cu/Al = 0.57). Compared with the Cu-SSZ-13 zeolite, the Cu-SSZ-39 zeolite was expected to be more stable owing to its topology and lower Si/Al ratio. The compositions of the two zeolites were optimized to balance NO_x conversion rate, hydrothermal stability, and selectivity.[7,35,36] We employed a multiscale approach to evaluate the impact of HTA on both the catalytic activity and structure of the zeolites. We used conventional structural characterization techniques (XRD and TEM) to obtain macroscopic information about the zeolites. We employed electron ptychography specifically to visualize changes in the zeolite at the atomic level. We combined these multiscale findings to elucidate the hydrothermal degradation mechanism.

The topologies of the two investigated zeolites are shown in Fig. 1a (CHA for SSZ-13) and Fig. 1b (AEI for SSZ-39). These structures differ in the linkage of the double six-membered ring (d6r) units, which are arranged in parallel in CHA and are connected *via* a mirror plane in AEI. Fig. 1c shows the two Cu sites in Cu-SSZ-13 at room temperature under ambient conditions, as has been reported on the basis of Rietveld refinement of XRD data.[37] The Cu ion at the d6r site (Fig. 1c, A site) is hydrothermally more stable than the eight-membered ring (8mr) site (Fig. 1c, B site), which is considered unstable.[7,8,38]

[a] Science & Innovation Center, Mitsubishi Chemical Corporation, 1000 Kamoshida-cho, Aoba-ku, Yokohama, Kanagawa, Japan
[b] Research Center for Energy and Environmental Materials, National Institute for Materials Science, 1-2-1 Sengen, Tsukuba, Ibaraki, Japan
[c] Graduate School of Science and Technology, University of Tsukuba, 1-2-1 Sengen, Tsukuba, Ibaraki, Japan
[d] Center for Basic Research on Materials, National Institute for Materials Science, 1-2-1 Sengen, Tsukuba, Ibaraki, Japan. E-mail: mitsuishi.kazutaka@nims.go.jp
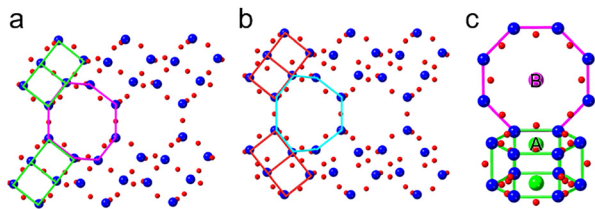
Fig. 1 Framework models of (a) SSZ-13 (CHA) and (b) SSZ-39 (AEI) viewed along the [100] direction. (c) Two Cu sites in Cu-SSZ-13 viewed perpendicular to the eight-membered ring (8mr) site:[37] the double six-membered ring (d6r; A, large green atom) and 8mr (B, large pink atom). To guide the eye, the d6r and 8mr sites are indicated by green and pink lines connecting Si atoms for SSZ-13, respectively, and by red and light-blue lines for SSZ-39, respectively. Element colors: Si (Al) = blue, O = red.

Similarly, Cu-SSZ-39 is reported to possess two distinct Cu sites analogous to those in Cu-SSZ-13.[5,39]

The hydrothermal stability of Cu-SSZ-13 and Cu-SSZ-39 was evaluated via standard NH$_3$-SCR activity tests. As shown in Fig. S1 (gas hourly space velocity = 2.0 × 10^5 h^{-1}), aging in the 150–500 °C temperature range decreased the average activity by 9.8% for Cu-SSZ-13 but by only 3.1% for Cu-SSZ-39. Thus, it was confirmed that both zeolites exhibited reduced activity due to aging, where the decrease in activity was smaller for Cu-SSZ-39 than for Cu-SSZ-13.

To clarify the structural changes induced by HTA, we first investigated the samples before and after aging using several conventional characterization techniques involving spatial averaging, including XRD, scanning electron microscopy-energy dispersion X-ray spectroscopy (SEM-EDS), and TEM. The XRD patterns of Cu-SSZ-13 and Cu-SSZ-39 (Fig. S2) contained the characteristic diffraction peaks for the respective frameworks. Comparison of the full widths at half maximum of selected peaks in the patterns obtained before and after HTA (Table S1) revealed no important differences for either zeolite, indicating that crystallinity of the framework was preserved upon aging. Similarly, no important changes were observed in the Cu distribution in the zeolites: SEM-EDS mapping showed that the Cu ions remained highly dispersed throughout the zeolite particles, regardless of hydrothermal treatment (Fig. S3). The TEM observations of the particle morphology (Fig. S4 and S5) revealed numerous faceted particles with single crystalline domains in both zeolites before and after HTA. Additionally, the aged samples did not appear to contain CuO$_x$ clusters,[5,40] which have been reported to form as a result of considerable hydrothermal degradation. Considering the results of these conventional characterization methods together shows that HTA produced no important changes in the framework crystallinity, interparticle elemental distribution, or particle morphology of either Cu-SSZ-13 or Cu-SSZ-39. This result suggests that the initial loss in catalytic activity was caused by more subtle structural alterations that were not discernible by the techniques used.

We subsequently employed electron ptychography to perform a detailed, atomic-scale structural analysis of five samples: fresh and hydrothermally aged Cu-SSZ-13 and Cu-SSZ-39

as well as Cu-free H-SSZ-13 as a reference for the visualization of Cu ions. The observation orientations were selected as the [100] directions in CHA and AEI, as shown in Fig. 1a and b (Fig. S6). Using this orientation made the d6r units align parallel to the electron beam, directly revealing the structural differences originating from the distinct linkage patterns of these units. Fig. S7–S11 show the ptychographic images acquired for the five samples over a field of view of approximately 10 nm square. It has been reported that large defocus in ptychographic images can cause internal pore artifacts.[33,34] Consequently, we carefully managed the defocus conditions to ensure that the ptychographic observations were reliable. We have previously demonstrated that under this observation condition, artifacts are negligible for defocus below 5 nm, allowing atomic columns containing Cu to be clearly distinguished from those without Cu.[33] Accordingly, we confirmed that the defocus for each reconstructed image was maintained below 5 nm (see the captions of Fig. S7–S11). To enhance the signal-to-noise ratio, a moving-average procedure was used to align and average approximately 20 equivalent sites for each sample.[41] The averaged images are presented in Fig. 2. The CHA framework (Fig. 1a) is clearly resolved in the image of the reference H-SSZ-13 (Fig. 2a). The image of the fresh Cu-SSZ-13 sample (Fig. 2b) contains distinct bright spots in the 8mr region (as indicated by the white arrow). These spots are assigned to Cu ions. This assignment is supported by the reconstructed defocus value of −1.4 nm (Fig. S12). By contrast, no such bright spots appear in the image of the sample subjected to HTA (Fig. 2c). A similar trend was observed for Cu-SSZ-39. The AEI framework is clearly resolved in the images of both the fresh (Fig. 2d) and aged (Fig. 2e) samples and is consistent with the model presented in Fig. 1b. The image of the fresh sample also contains bright spots in the 8mr region, which are assignable to Cu ions (reconstructed defocus: +1.4 nm; Fig. S13). However, these spots are absent in the image of the aged sample. Direct visualization of Cu ions at the d6r sites proved inconclusive, primarily because of strong overlap between the Cu ions and Si (Al) atomic columns in the chosen projection (Fig. S14). This challenge was particularly pronounced for the AEI structure, which lacks an alternative zone axis that can enable clear d6r observation. The averaged and original nonaveraged images (Fig. S7–S11) yielded consistent key results for the 8mr sites—namely, the presence of Cu ions in the fresh samples and the absence of these ions in the aged samples.

To determine the relative quantity of Cu ions at the 8mr sites of the two zeolites and how this quantity changes upon HTA, we compared the contrast values of the five samples. In ptychography, the retrieved phase contrast increases with the projected potential of the sample, provided that the phase shift of electron wave remains below 2π. Considering that no phase inversion was observed for the Si (Al) columns, the relative quantity of Cu ions at the 8mr sites was determined by comparing the contrast for the five samples. Fig. 3 shows the line profiles obtained from the averaged ptychographic images of the five samples shown in Fig. 2. The extracted region corresponds to the area between two O atomic columns
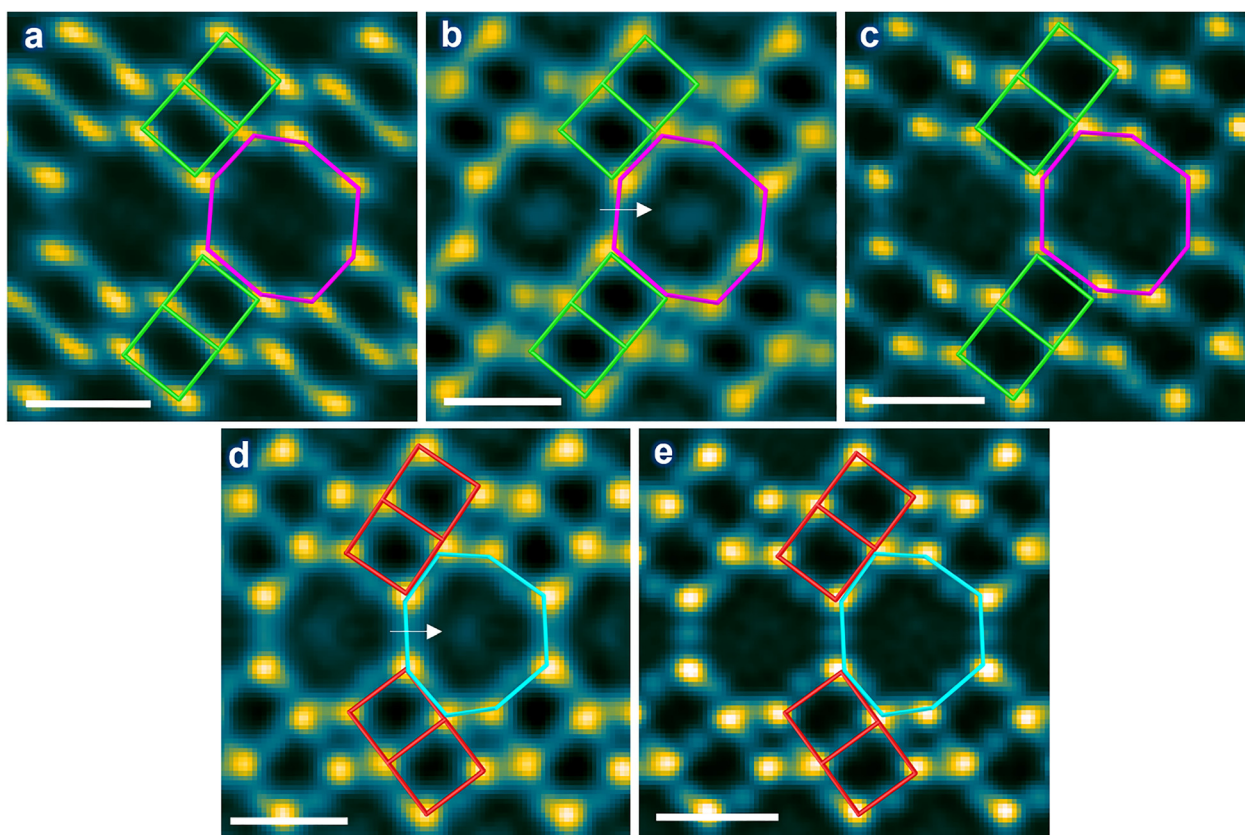
Fig. 2 Ptychographic images viewed along the [100] direction of (a) H–SSZ-13 (without Cu), (b) Cu-SSZ-13, (c) Cu-SSZ-13-HTA, (d) Cu-SSZ-39, and (e) Cu-SSZ-39-HTA. All the images were subjected to moving averaging by performing alignment and averaging over approximately 20 sites. The white arrows indicate areas of bright spots in the eight-membered ring (8mr) region of both zeolites before hydrothermal aging (HTA). Scale bar: 0.5 nm.

(delineated by the red box) in the SSZ-13 (CHA) and SSZ-39 (AEI) models viewed along the [100] direction, as illustrated in
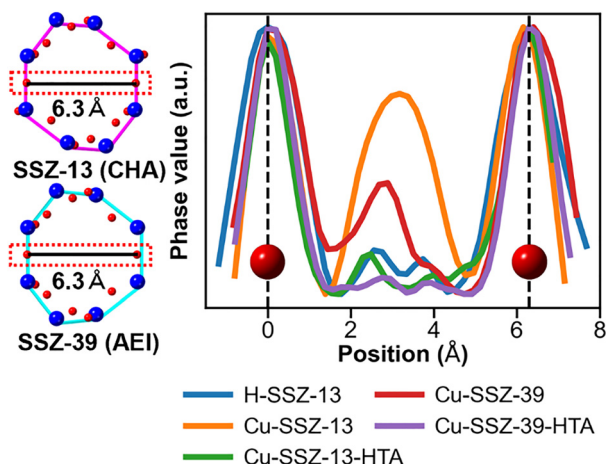

Fig. 3 Line profiles for the eight-membered ring (8mr) region obtained from the ptychographic images shown in Fig. 2. The line profiles were acquired for the regions between the two O atomic columns indicated by the red boxes in the inset (left). The values on the vertical axis were normalized using the maximum and minimum values for each line profile. The origin of the horizontal axis is placed at one O column. The unnormalized profiles showing identical relative trends for the samples are provided in Fig. S15.

the inset (left) of Fig. 3. In the line profile of H-SSZ-13, a weak peak appears near the center between the O columns. This peak is presumed to mainly result from contributions from adsorbed volatile organic compounds or a surface amorphous layer produced by beam damage. In the line profile of the fresh Cu-SSZ-13 sample, the large peak near the center between the two O columns can be interpreted as originating from Cu ions, as mentioned above. Notably, the high peak intensity for the line profile of the fresh Cu-SSZ-13 sample decreases in the line profile of the aged sample. The peak intensity for the aged sample profile is similar to that of H-SSZ-13, indicating a substantial reduction of Cu ions in the 8mr upon aging. Similar behavior is observed for Cu-SSZ-39: the 8mr center contrast for the fresh sample exceeds that of H-SSZ-13, suggesting the presence of Cu ions; however, the 8mr center contrast for the aged sample is comparable to that of H-SSZ-13, again indicating Cu loss from the 8mr. The contrast for the 8mr region in the aged sample was higher for Cu-SSZ-13 than for Cu-SSZ-39. Both samples were prepared to have similar Cu contents. In previous studies,[5,38,42] Cu sites were reported to be either 8mr or d6r. Therefore, the Cu-SSZ-39 sample studied here has a lower Cu occupancy at the 8mr site than Cu-SSZ-13. That is, Cu-SSZ-39 can be considered to have a higher Cu occupancy at the d6r site than Cu-SSZ-13.

Next, we present a mechanism for hydrothermal degradation on the basis of our experimental results. Although the activity tests indicated differing stabilities for the two zeolites, no structural changes reflecting different degradation levels were detected using the conventional techniques. By contrast, atomic-scale electron ptychography clearly revealed a reduction in the Cu ion occupancy at the 8mr sites after aging. A key finding is that the less stable Cu-SSZ-13 contained a higher initial quantity of Cu ions at these 8mr sites than the more stable Cu-SSZ-39. This observation supports previous reports proposing that these mobile 8mr ions migrate to form framework-disrupting CuO_x clusters.[5,7,9] Therefore, the loss of Cu ions from the 8mr sites can be interpreted as the onset of a structural response to HTA.

In this study, electron ptychography was used to visualize early hydrothermal degradation at the atomic level. Subtle changes in the Cu ion occupancy at the 8mr sites were successfully captured using this technique, whereas no structural changes were observed using XRD or conventional TEM. These findings provide concrete, atomic-scale evidence for the proposed degradation mechanism, going beyond previous inferences from spatially-averaged data.[14,15] Considering that the 8mr and d6r Cu sites are known to differ not only in hydrothermal stability but also in activity and selectivity,[5,9] a multiscale approach including electron ptychography provides guidelines for the rational design of highly durable and high-performance zeolites based on control of the arrangement of Cu ions.

Conflicts of interest

There are no conflicts to declare.

Data availability

The data supporting this article have been included as part of the supplementary information (SI). Supplementary information: sample preparation, activity test conditions, characterization conditions, and figures/a table for material characterizations. See DOI: https://doi.org/10.1039/d5cc06274h.

References

1 A. M. Beale, F. Gao, I. Lezcano-Gonzalez, C. H. F. Peden and J. Szanyi, *Chem. Soc. Rev.*, 2015, **44**, 7371–7405.
2 J. H. Kwak, R. G. Tonkyn, D. H. Kim, J. Szanyi and C. H. F. Peden, *J. Catal.*, 2010, **275**, 187–190.
3 F. Gao, J. H. Kwak, J. Szanyi and C. H. F. Peden, *Top. Catal.*, 2013, **56**, 1441–1459.
4 C. Paolucci, A. A. Parekh, I. Khurana, J. R. Di Iorio, H. Li, J. D. Albarracin Caballero, A. J. Shih, T. Anggara, W. N. Delgass, J. T. Miller, F. H. Ribeiro, R. Gounder and W. F. Schneider, *J. Am. Chem. Soc.*, 2016, **138**, 6028–6048.
5 Y. Shan, W. Shan, X. Shi, J. Du, Y. Yu and H. He, *Appl. Catal., B*, 2020, **264**, 118511.
6 T. Usui, Z. Liu, H. Igarashi, Y. Sasaki, Y. Shiramata, H. Yamada, K. Ohara, T. Kusamoto and T. Wakihara, *ACS Omega*, 2019, **4**, 3653–3659.
7 Y. J. Kim, J. K. Lee, K. M. Min, S. B. Hong, I.-S. Nam and B. K. Cho, *J. Catal.*, 2014, **311**, 447–457.
8 F. Gao and J. Szanyi, *Appl. Catal., A*, 2018, **560**, 185–194.
9 J. Song, Y. Wang, E. D. Walter, N. M. Washton, D. Mei, L. Kovarik, M. H. Engelhard, S. Prodinger, Y. Wang, C. H. F. Peden and F. Gao, *ACS Catal.*, 2017, **7**, 8214–8227.
10 C. W. Andersen, E. Borfecchia, M. Bremholm, M. R. V. Jørgensen, P. N. R. Vennestrøm, C. Lamberti, L. F. Lundegaard and B. B. Iversen, *Angew. Chem., Int. Ed.*, 2017, **56**, 10367–10372.
11 M. Moliner, C. Franch, E. Palomares, M. Grill and A. Corma, *Chem. Commun.*, 2012, **48**(66), 8264–8266.
12 N. Martín, C. R. Boruntea, M. Moliner and A. Corma, *Chem. Commun.*, 2015, **51**, 11030–11033.
13 J. D. Albarracin-Caballero, I. Khurana, J. R. D. Iorio, A. J. Shih, J. E. Schmidt, M. Dusselier, M. E. Davis, A. Yezerets, J. T. Miller, F. H. Ribeiro and R. Gounder, *React. Chem. Eng.*, 2017, **2**, 168–179.
14 Y. Shan, J. Du, Y. Zhang, W. Shan, X. Shi, Y. Yu, R. Zhang, X. Meng, F.-S. Xiao and H. He, *Natl. Sci. Rev.*, 2021, **8**, nwab010.
15 G. Fu, R. Yang, Y. Liang, X. Yi, R. Li, N. Yan, A. Zheng, L. Yu, X. Yang and J. Jiang, *Microporous Mesoporous Mater.*, 2021, **320**, 111060.
16 J. M. Thomas and G. R. Millward, *J. Chem. Soc., Chem. Commun.*, 1982, 1380–1383.
17 T. Ohsuna, O. Terasaki and K. Hiraga, *Mater. Sci. Eng. A*, 1996, **217–218**, 135–138.
18 S. X. Wang, L. M. Wang and R. C. Ewing, *J. Nucl. Mater.*, 2000, **278**, 233–241.
19 O. Ugurlu, J. Haus, A. A. Gunawan, M. G. Thomas, S. Maheshwari, M. Tsapatsis and K. A. Mkhoyan, *Phys. Rev. B: Condens. Matter Mater. Phys.*, 2011, **83**, 113408.
20 A. Mayoral, Q. Zhang, Y. Zhou, P. Chen, Y. Ma, T. Monji, P. Losch, W. Schmidt, F. Schüth, H. Hirao, J. Yu and O. Terasaki, *Angew. Chem., Int. Ed.*, 2020, **59**, 19510–19517.
21 W. Hoppe, *Acta Crystallogr.*, 1969, **25**, 67–76.
22 T. J. Pennycook, A. R. Lupini, H. Yang, M. F. Murfitt, L. Jones and P. D. Nellist, *Ultramicroscopy*, 2015, **151**, 160–167.
23 J. Rodenburg and R. Bates, *Philos. Trans. R. Soc., A*, 1992, **339**, 521–553.
24 C. M. O'Leary, C. S. Allen, C. Huang, J. S. Kim, E. Liberti, P. D. Nellist and A. I. Kirkland, *Appl. Phys. Lett.*, 2020, **116**, 124101.
25 H. Zhang, G. Li, J. Zhang, D. Zhang, Z. Chen, X. Liu, P. Guo, Y. Zhu, C. Chen, L. Liu, X. Guo and Y. Han, *Science*, 2023, **380**, 633–638.
26 Z. Dong, E. Zhang, Y. Jiang, Q. Zhang, A. Mayoral, H. Jiang and Y. Ma, *J. Am. Chem. Soc.*, 2023, **145**, 6628–6632.
27 H. Sha, J. Cui, J. Li, Y. Zhang, W. Yang, Y. Li and R. Yu, *Sci. Adv.*, 2023, **9**, eadf1151.
28 G. Li, M. Xu, W.-Q. Tang, Y. Liu, C. Chen, D. Zhang, L. Liu, S. Ning, H. Zhang, Z.-Y. Gu, Z. Lai, D. A. Muller and Y. Han, *Nat. Commun.*, 2025, **16**, 914.
29 Y. Jiang, Z. Chen, Y. Han, P. Deb, H. Gao, S. Xie, P. Purohit, M. W. Tate, J. Park, S. M. Gruner, V. Elser and D. A. Muller, *Nature*, 2018, **559**, 343–349.
30 H. Yang, R. N. Rutte, L. Jones, M. Simson, R. Sagawa, H. Ryll, M. Huth, T. J. Pennycook, M. L. H. Green, H. Soltau, Y. Kondo, B. G. Davis and P. D. Nellist, *Nat. Commun.*, 2016, **7**, 12532.

31 S. Gao, P. Wang, F. Zhang, G. T. Martinez, P. D. Nellist, X. Pan and A. I. Kirkland, *Nat. Commun.*, 2017, **8**, 163.

32 J. G. Lozano, G. T. Martinez, L. Jin, P. D. Nellist and P. G. Bruce, *Nano Lett.*, 2018, **18**, 6850–6855.

33 K. Mitsuishi, K. Nakazawa, R. Sagawa, M. Shimizu, H. Matsumoto, H. Shima and T. Takewaki, *Sci. Rep.*, 2023, **13**, 316.

34 M. Shimizu, K. Nakazawa, H. Shima, M. Koike, H. Matsumoto, T. Takewaki, K. Mitsuishi and A. Hashimoto, *ChemistrySelect*, 2026, **11**(1), e03562.

35 T. Pham, J. Lu, J. Fedeyko, R. Lobo and H.-Y. Chen, *25th North American Catalysis Society Meeting*. NAM, 2017.

36 D. Yao, B. Liu, F. Wu, Y. Li, X. Hu, W. Jin and X. Wang, *Ind. Eng. Chem. Res.*, 2021, **60**, 10083–10093.

37 A. M. Beale, I. Lezcano-Gonzalez, W. A. Slawinksi and D. S. Wragg, *Chem. Commun.*, 2016, **52**, 6170–6173.

38 C. W. Andersen, M. Bremholm, P. N. R. Vennestrøm, A. B. Blichfeld, L. F. Lundegaard and B. B. Iversen, *IUCrJ*, 2014, **1**, 382–386.

39 B. Ipek, M. J. Wulfers, H. Kim, F. Göltl, I. Hermans, J. P. Smith, K. S. Booksh, C. M. Brown and R. F. Lobo, *ACS Catal.*, 2017, **7**, 4291–4303.

40 L. Ma, Y. Cheng, G. Cavataio, R. W. McCabe, L. Fu and J. Li, *Chem. Eng. J.*, 2013, **225**, 323–330.

41 L. Jones, H. Yang, T. J. Pennycook, M. S. J. Marshall, S. Van Aert, N. D. Browning, M. R. Castell and P. D. Nellist, *Adv. Struct. Chem. Imaging*, 2015, **1**, 8.

42 J. H. Kwak, H. Zhu, J. H. Lee, C. H. F. Peden and J. Szanyi, *Chem. Commun.*, 2012, **48**, 4758–4760.